Estimation of gyro bias drift due to distributed polarization cross coupling in the fiber coil

YUANHONG YANG,[1] HAN YAN,[1] SHUAI LI,[1] FULING YANG,[1] AND WEI JIN[2,*]

[1]*Beihang University, School of Instrumentation and Optoelectronics Engineering, Beijing 100191, China*
[2]*The Hong Kong Polytechnic University, Department of Electrical Engineering, Hong Kong, China*
*wei.jin@polyu.edu.hk

Abstract: Distributed polarization cross coupling (PCC) along the polarization-maintaining fiber (PMF), obtained from an optical coherence domain polarimetry (OCDP) system, is analyzed. It is found that the measured PCC data at each measurement location is the sum of the OCDP source coherence function centered at a series of discrete PCC points, which do not represent the true PCC information. An algorithm is developed to extract the "true" location and strength of the PCC and the extracted PCC data are no longer source dependent. A model is developed to relate the extracted PCC data in the PMF coil to the fiber optic gyro (FOG) bias drift due to coherent PCC. Experimental results obtained with a FOG with a ~3 km PMF coil and light sources of different bandwidths agree with the theoretically estimated bias drifts.

1. Introduction

Phase nonreciprocal error (PNR) due to polarization cross coupling (PCC) in the fiber coil imposes a limit on the precision of fiber optic gyroscopes (FOGs) [1]. The use of polarization-maintaining fibers (PMFs) and multifunctional integrated optical circuit (MIOC) provides a good solution to tightly control the state of polarization [2]. However, the residual distributed PCC induced during the fabrication of the PMF coil is still a significant source of PNR that affects the performance of FOGs [3].

Optical coherence domain polarimetry (OCDP) is a well-established technique that can be used to measure the distributed PCC in a PMF with high sensitivity and high spatial resolution [4,5]. In 1986, Takada et al. firstly reported the measurement of the spatial distribution of mode coupling along a PMF with an optical coherence domain technique [6]. In 1991, Kemmler et al. reported the test of FOG components with white light interferometry [7]. Recently, a number of research groups have used OCDP systems to measure the PCC in PMFs, connectors, splices, and integrated optical components [8,9]. General Photonics Corporation [10], Harbin Engineering University [11] and some other research groups [12,13] have successfully developed high performance OCDP systems and some of these instruments are now commercially available. However, most of the work reported so far focuses on improving the OCDP systems to achieve better sensitivity, spatial resolution and measurement range [14,15]. A quantitative analysis of the distributed PCC data and its relationship to the performance of the FOG have not been well performed as far as we know.

In this paper, we report quantitative estimation of FOG bias drift based on the distributed PCC data of the PMF coil obtained by use of an OCDP system. In Section 2, we analyze the measured distributed PCC data and conclude that the measured PCC ratio at each measurement location is the sum of the OCDP source coherence functions centered at a series of discrete PCC points and it may not be the true PCC information (i.e., coupling ratio and location). In section 3, we present an algorithm to extract the effective PCC data pairs from the raw measurement data and the extracted data are source independent and may be regarded as the "true" PCC ratio and location. In section 4, we report a model to estimate the FOG bias

drift due to coherent mixing of the polarization coupled waves with the main waves, and use it to estimate quantitatively the bias drift of the FOG based on the extracted PCC data. In section 5, the bias drifts were measured and the experimental results support the results of the theoretical modeling. The algorithm and model described in this paper may be used for quality evaluation of PMF coils as well as quantitative estimation of the gyro bias drift.

2. Analysis of PCC data

A: PCC point, O: Output end of PMF Coil, M: Main wave train, C: Coupled wave train, BS: Beam Splitter, FM: Fixed Mirror, SM: Scanning Mirror
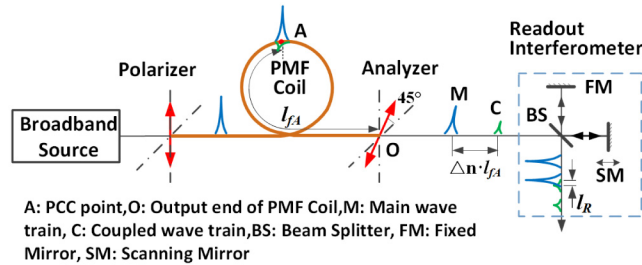
Fig. 1. Schematic showing the basic principle of OCDP.

The basic configuration of an OCDP system is shown in Fig. 1. It consists of a broadband source, a polarizer, an analyzer, a PMF coil, and a readout interferometer. The readout interferometer is a scanning Michelson interferometer, consisting of a beam splitter (BS), a fixed mirror (FM), a scanning mirror (SM) that changes the optical path difference (OPD) with a step size of S_R. Light from the broadband source is linearly polarized after polarizer and injected into the PMF coil alone one of its principal axes. When there is a PCC point (marked as A) located at l_{fA} (the fiber length between the PCC point A and output end O) of the PMF coil, a fraction of light is coupled to the orthogonal polarization state. Because of birefringence, the main and coupled wave trains (labeled as M and C respectively) travel through the PMF coil at different velocities. At the output of the PMF, the OPD between the main and the coupled waves is $\Delta n \cdot l_{fA}$, where Δn is the birefringence of the PMF. The analyzer, oriented at 45° of the PMF's principal axes, placed at the output of the PMF coil, projects the two wave-trains onto the same state of polarization. Interference will happen between them when the OPD (l_R) of the readout interferometer matches to that between main and the coupled waves. There will be interference maximums when l_R is $-\Delta n \cdot l_{fA}$, 0 and $+\Delta n \cdot l_{fA}$, respectively, as shown in Fig. 2.
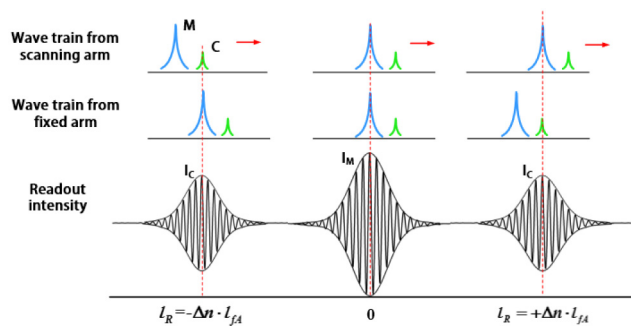

Fig. 2. Readout intensity for one coupling point in the PMF coil.

The three interference peaks at the output of the readout intensity correspond to the self-interference (middle peak, noted as I_M) of main wave train and inter-interference between main and coupled wave trains (left and right peaks, noted as I_C). In the OCDP, the readout interferometer was designed in such a way that only one of the two inter-interferences is

taken out to calculate the PCC ratio [16]. For a single PCC point A, the coupling amplitude radio ρ_A may be obtained by [5]:

$$\rho_A = \frac{I_C(l_{fA})}{I_M}.$$ (1)

Figure 3 illustrates the typical PCC data ρ_q (red dot) for one PCC point measured at location l_{fq} by use of an OCDP system with OPD scanning step S_R. Because of the limited spectrum width of the broadband source, the envelope of ρ_q, for a single PCC point, resembles that of the coherence function of the light source and can be expressed as:

$$\rho(l_f) = \rho_A \cdot \gamma(\Delta n(l_f - l_{fA})) = \rho_A \cdot \exp\{-[\Delta n(l_f - l_{fA})/2l_c]^2\},$$ (2)

where $\gamma(x)$ represents the normalized coherence function of the source, which is approximated here as a Gaussian function. l_c is the coherence length of the source. ρ_A is the coupling amplitude radio at PCC point A as described in Eq. (1). In Fig. 3, we used two horizontal axes. One (l_R) represents the OPD of the readout interferometer, the another represents the corresponding fiber length (l_f) between the coupling point and the PMF coil end, and they are related by $l_f = l_R/\Delta n$. l_{dc} in Fig. 3 represents the de-coherence length of broadband source and is defined as the value of coherence function reduced to 3% of its maximum value. l_d is the corresponding de-coherence parameter in terms of the PMF length.

In the OCDP system, the scanning step S_R is less than one micro meter and the PCC data was obtained at each scanning location. So, there will be multiple PCC data within the range of de-coherence length, as shown in Fig. 3. The output data from the OCDP system may be written as:

$$\rho_q = \rho_A \cdot \gamma(qS_R - \Delta n \cdot l_{fA}) = \rho_A \cdot \exp\{-[(qS_R - \Delta n \cdot l_{fA})/2l_c]^2\},$$ (3)

where q is the serial number of measured data. The output data from OCDP is often expressed in logarithmic scale:

$$P_q = 20\lg(\rho_q).$$ (4)

It is obviously that the PCC data (ρ_q) is the nearest to the PCC point A, which may be used to represent the PCC amplitude ratio ρ_A and other data (i.e., ρ_{q+1}, ρ_{q-1}, ρ_{q+2}, ρ_{q-2},...) do not provide extra information.
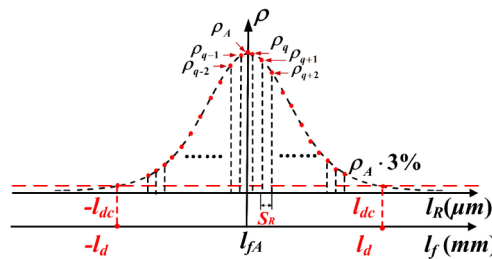

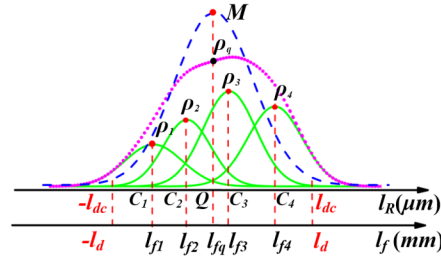Fig. 3. Schematic showing the output from an OCDP system for one PCC point.

Fig. 4. Schematic showing the output from an OCDP system for multiple PCC points within the de-coherence length.

Figure 4 shows the schematic OCDP output for m ($m = 4$, for example) PCC points (C_i) at location l_{fi} ($i = 1$ to 4) within a de-coherence length $\pm l_d$. The blue dash line corresponds the main wave train at the measuring location l_{fq}, the solid green lines represent the coherence function centered at the four different PCC points. There will be multiple interferences between the main wave M and the coupled waves C_i ($i = 1,2,…,m$). Assuming the PCC ratio at location C_i is ρ_i, then the measured PCC data with serial number q at location $l_{fq} = q \cdot S_R / \Delta n$ may be expressed as:

$$\rho_q = \sum_{i=1}^{m} \rho_i \cdot \gamma[\Delta n(l_{fq} - l_{fi})], \quad (0 < |l_{fq} - l_{fi}| < l_d). \tag{5}$$

As shown in Fig. 4, the magenta dot line shows the envelope of measured data within the de-coherence length $\pm l_d$. It is the sum of m multiple coherence functions as described by Eq. (5). Similar to the case of single PCC, these data depend on the coherence function $\gamma(x)$ of source and there should be only one pair of PCC data representing the PCC ratio ρ_i and they need to be extracted from the raw PCC data with a special algorithm. In the following section, we describe such an algorithm from which the effective or "true" location and coupling ratio (l_{fi}, ρ_i) of PCC in the PMF coil can be extracted by use of the measured raw PCC data pairs (l_{fq}, ρ_q).

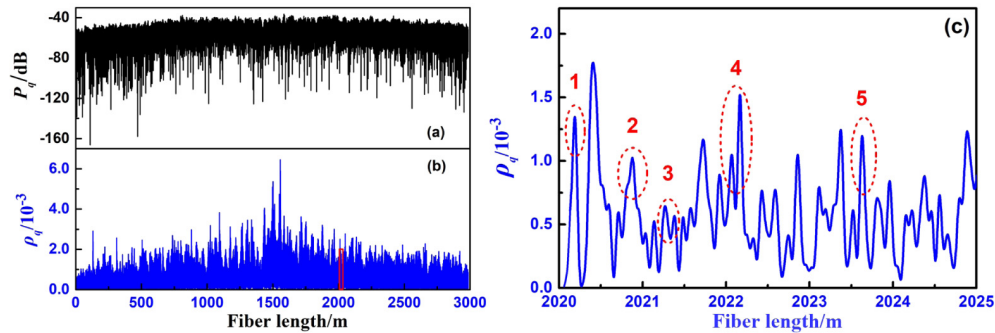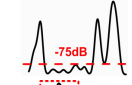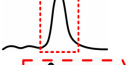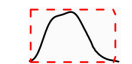## 3. Extraction algorithm for effective PCC points

Fig. 5. Measured PCC data along a ~3-km-long PMF coil. (a) logarithmic scale, (b) linear scale, (c) zoom-in of red frame in (b).

Figure 5 shows a typical set of measured distributed PCC data along a ~3 km long PMF coil and the number of data points reaches up to 930000. The PCC data were obtained by using of a commercial OCDP instrument (OCDP-F-SLD-1550nm) developed by Harbin Engineering University, China. The instrument uses a special range extension technique, which enables measurements over a long fiber length of up to 5 km [17,18]. The same set of PCC data is shown in logarithmic scale (Fig. 5(a)) and linear scale (Fig. 5(b)). Figure 5(c) is an enlarged

view of data points over the region from 2020 to 2025 m, corresponding to range within the red rectangle in Fig. 5(b).

Table 1. PCC data partition

Case No.	Typical legend	Basic criterion	Number of PCC Points
1		The background noise below-75dB	-
2		Single PCC points& w≈$2l_d$	1
3		Multi distinct peaks & $(m + 1)$ l_d≦w≦$2m$ l_d	m,(m>1)
4		Broad peak or flattop & $2l_d$<w <$(m + 1)l_d$	m,(m>1)

As shown in Fig. 5(c), there are different PCC distributions and we may classify them into different cases. For example, there may be a single PCC point for PCC distribution 1, 5 and multiple PCC points for 2, 3 and 4. To extract the effective PCC data, the raw PCC data are described with serial data pair (l_{fq}, ρ_q) and partitioned into four main cases with typical legends shown in Table 1, where l_{fq} and ρ_q represent respectively the PCC measurement location and the corresponding amplitude ratio along the PMF, w is the width of peak at about −15 dB (~3%) of the maximum value.

Case 1: Background noise. The strength of the PCC is less than or equal to the initial PCC in the PMF before winding to form the gyro coil, which is about −75dB and can be removed directly to reduce the number of data set for further processing.

Case 2: Single peak. There is only one PCC point within ± l_d width, the PCC data pair (l_{fi}, ρ_i) can be picked up directly.

Case 3: Overlapped multiple distinct peaks. When the space between neighbor PCC points is larger than l_d and less than $2l_d$, m (m>1) distinct peaks would appear. The overall width of the overlapped peaks is larger than $(m + 1)$ l_d and less than $2ml_d$. Then, 2m data pairs will be selected from the raw PCC data to form 2m equations to extract effective data pair (l_{fi}, ρ_i).

Case 4: Broad peak or flattop. When there are m (m>1) PCC points and the space between neighbor PCC points is less than l_d, the PCC profile may be a broad peak or flattop and the overall width of the profile is larger than $2l_d$ and less than $(m + 1)l_d$, a suitable number of data pairs with equal length interval will be selected to form the equation groups.

Base on above analysis, we develop an effective PCC points extraction algorithm and the flow chart is shown in Fig. 6.
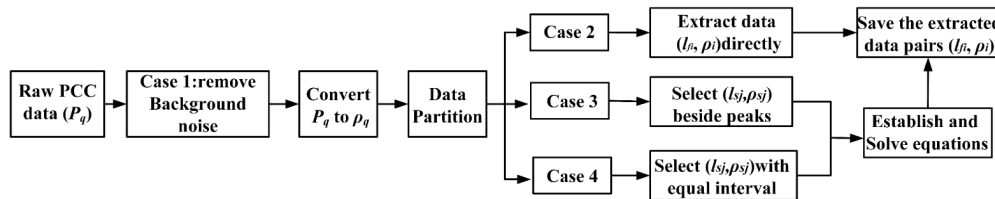

Fig. 6. Flow chart of the extraction algorithm.

After removing the background noise data (Case 1: P_q<-75dB) from the raw PCC data, we then convert PCC data P_q (logarithmic scale) to ρ_q (linear scale) and portition the data to the three other cases in numerical order. For Case 2, the peak data pair (l_{fq}, ρ_q) can be picked up directly as the effective data pair (l_{fi}, ρ_i). For Case 3 and Case 4, multiple data pairs are

selected to form equation groups to solve data pair (l_{fi}, ρ_i). For any other cases, which happen infrequently, we may treat them the same as Case 4.

Finally, the extracted data (l_{fi}, ρ_i) were saved as the effective PCC data. As listed in Table 1, for case 3, there are m distinct peaks within $(m + 1) l_d \leq w \leq 2ml_d$, there may be m effective PCC points and $2m$ PCC pairs (l_{sj}, ρ_{sj}), $(j = 1,2,..,2m)$ can be selected at near middle position besides each peak. For example, when $m = 3$, the 6 data pairs can be selected as shown in Fig. 7. For case 4, the profile is broad and it is not easy to see distinct peaks, the number m can be determined by using the following equation:

$$m = [w / 2l_d] + 1, \qquad (6)$$

where $[x]$ is a floor function. The $2m$ special PCC pairs (l_{sj}, ρ_{sj}) will be selected with equal interval of $w/(2m + 1)$. Figure 8 shows the selected sample data pairs for $m = 3$.
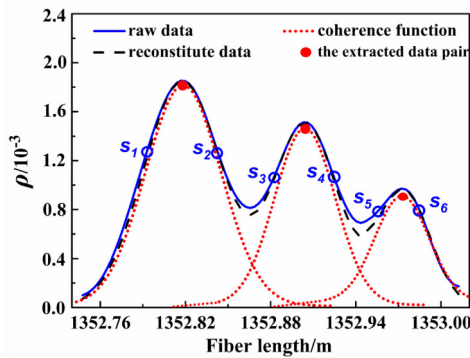

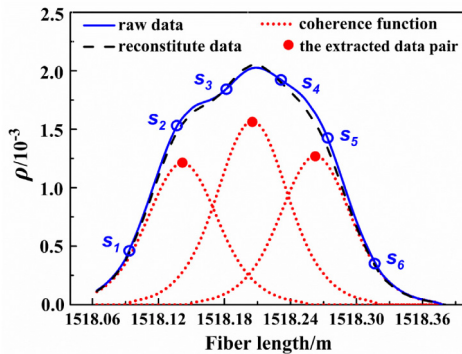Fig. 7. Typical measured and fitted results for case 3.

Fig. 8. Typical measured and fitted results for case 4.

For Cases 3, 4 and other infrequent cases, by using Eq. (5), we can get $2m$ equations with the selected $2m$ data pairs (l_{sj}, ρ_{sj}), $(j = 1,2,..,2m)$ as:

$$\rho_{sj} = \sum_{i=1}^{m} \rho_{fi} \exp\{-[\Delta n(l_{sj} - l_{fi}) / 2l_c]^2\}. \qquad (7)$$

By using Fig. 7, the m effective PCC data pairs (l_{fi}, ρ_i) $(i = 1,2,..,m)$ can be solved out. Figures 7 and 8 are exemplary traces of Case 3 and Case 4, respectively, which were taken from the raw data in Fig. 5. In Fig. 7, there are 3 distinct peaks and 6 data pairs are selected besides each peak and marked as $s_1, s_2 ..., s_6$. The main parameters of the SLD used in the

OCDP system are listed in Table 2 where λ is the average wavelength of source and $\Delta\lambda$ is its spectrum width. The solved effective PCC data pairs are listed in Table 3.

Table 2. The main parameters of the OCDP

λ (nm)	$\Delta\lambda$ (nm)	l_c (μm)	l_{dc} (μm)	Δn (10^{-4})	l_d (mm)	S_R(μm)
1548.94	46.52	12.7	48.2	6.01	80.3	0.96

The typical results for Case 3 and Case 4 and m = 3 are shown in Fig. 7 and Fig. 8 respectively. The extracted effective PCC data pairs are listed in Table 3 and Table 4 and these may be regarded as the actual PCC data. To verify the results further, the source coherence function curves centered at each PCC points are simulated with Eq. (3) and plotted (red dotted line) independently. Their sum was calculated with Eq. (5) and the reconstructed curve (black dash line) fits the raw data (blue solid line) very well.

Table 3. The extracted results of case 3

Peak No.	Raw peak	Solved result
1	(1352.818m, 1.848 × 10^{-3})	(1352.819m, 1.784 × 10^{-3})
2	(1352.903m, 1.514 × 10^{-3})	(1352.903m, 1.448 × 10^{-3})
3	(1352.972m, 0.971 × 10^{-3})	(1352.973m, 0.896 × 10^{-3})

Table 4. The extracted results of case 4

Peak No.	Raw peak	Solved result
1		(1518.141m, 1.210 × 10^{-3})
2	(1518.208m, 2.027 × 10^{-3})	(1518.205m, 1.572 × 10^{-3})
3		(1518.262m,1.271 × 10^{-3})

Taking raw PCC data of the ~3 km sample coil as input, only 23244 effective PCC data pairs have been extracted from 930000 raw data. This means that there are only 23244 actual "true" PCC points in the PMF coil and these extracted PCC data are no longer source dependent.
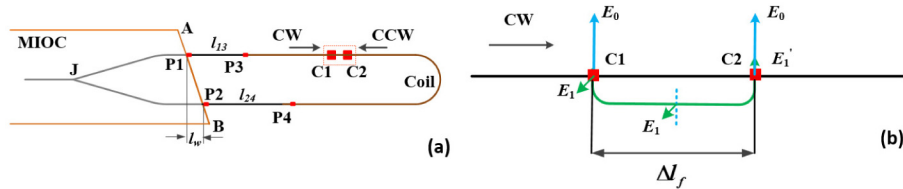
4. Estimation of gyro bias drift

Fig. 9. Schematic structure of SIA assembly. (a) Simplified PMF SIA with two PCC. (b) Zoom in of two PCC section.

Figure 9(a) is a schematic of the Sagnac interferometer assembly (SIA) of FOG with a PMF coil, where line AB is the slant interface of multifunction integration optic circuit (MIOC). The assembly is composed of three parts, the waveguide segments (J-P1 and J-P2), the PMF pigtails (P1-P3 and P2-P4), and the PMF coil. There may be possible parasitic Michelson interferometer formed by back reflections as well as polarization coupling at P1 to P4 due to misalignment of the principal axes of the MIOC and the PMFs. But this phase error can be suppressed more than 80 dB [19] by using high polarization extinction MIOC and setting $n_w l_w > l_{dc}$ and $l_{24} - l_{13} > l_{dc}$, where n_w is the refractive index of waveguide. l_w is the path

imbalance between the two branches of the MIOC, and l_{24}, l_{13} are the lengths of the two pigtails. Since the polarization extinction ratio of the MIOC is sufficiently and l_{13}, $l_{24}>>l_d$, the PNR due to PCC at P1-P4 may be regarded as negligible level. Hence, the phase error in this SIA may be considered mainly due to parasitic interference between the coupled waves at the PCC points where the distance between them are less than l_d in the PMF coil.

The parasitic interference in the PMF may be understood with the aid of Fig. 9, where C1, C2 are the PCC points in the PMF coil and their PCC amplitude ratios are ρ_1 and ρ_2 respectively. When the main wave E_0 propagates clockwise (CW) in the sensing coil, the first PCC will occur at C1 and produces coupled wave E_1. At C2, E_1 is coupled back to the original polarization state, resulting in a second order coupled wave with amplitude E_1'. The interference between this second order coupled wave E_1' and main wave E_0 results in bias drift to FOG. There may be higher order PCC in PMF coil but they are small enough to be ignored. Assuming the distance between C1and C2 is Δl_f, the corresponding phase difference δ between the main and the second order coupled waves may be expressed as:

$$\delta = \frac{2\pi}{\lambda} \cdot \Delta n \cdot \Delta l_f, \tag{8}$$

where λ represents the mean wavelength of light source used in the FOG. The PCC ratio of the second order coupling is $\rho' = (\rho_1\rho_2)^{1/2}$. By the following a similar process as in [19], we can estimate the magnitude of interference between the main and the second order coupled waves. The nonreciprocal phase error due to this second order coherent PCC may be expressed as:

$$\varphi_e \approx 2 \cdot \rho' \cdot \sin(\delta) \cdot \gamma(\Delta l_f). \tag{9}$$

If there are N pairs of PCC points in the PMF coil with distance between them less than l_d, the total phase error may be rewritten as:

$$\varphi_{te} \approx \sum_1^N 2 \cdot \rho_i' \cdot \sin(\delta_i) \cdot \gamma(\Delta l_{fi}). \tag{10}$$

Assuming the gyroscope scale factor is K, the bias drift due to these parasitic interferences may be determined as:

$$\Omega_{ED} = K \cdot \varphi_{te}. \tag{11}$$

With the extracted PCC data in Section 3, the bias drift of the FOG due to the coherent PCC in the PMF coil may be estimated by use of an algorithm described as follows:

Step 1: Calculate the parameters of l_c and l_d by use of the spectral data of the source and the birefringence of the PMF used in the FOG and constructive the coherence function $\gamma(\Delta l_f)$.

Step 2: Pick up coherent pairs of the PCC serially in all effective PCC data and calculate the total phase error with Eqs. (8)–(10).

Step 3: Use scale factor K of the FOG to calculate bias drift with Eq. (11).

Table 5. The estimated Ω_{ED} and measured bias drift with different sources under room temperature

Source	$\overline{\lambda}$ (nm)	$\Delta\lambda$ (nm)	Ω_{ED} (°/h) With raw data	Ω_{ED} (°/h) With extracted data	Measured bias drift (°/h)
SFS1	1531.23	6.81	7.83×10^{-2}	8.98×10^{-4}	1.695×10^{-3}
SFS2	1563.31	13.38	6.34×10^{-2}	6.57×10^{-4}	1.022×10^{-3}
SFS3	1544.13	27.62	5.93×10^{-2}	5.13×10^{-4}	0.774×10^{-3}
SLD	1548.94	46.52	4.21×10^{-2}	3.86×10^{-4}	-

With the above algorithm, the bias drifts of a FOG with the 3 km PMF coil powered by four different sources, i.e., the SLD used in OCDP and three different superfluorescent fiber sources (SFSs), are estimated. The SFSs are based on amplified spontaneous emission of

erbium-doped fibers, with their center wavelengths and spectral widths listed in Columns 2 and 3 of Table 5.

The PMF coil has a length of 2987.4 m and an average coil diameter is 165mm. The fiber coil has 76 layers made by quadrupole symmetrical winding technique, giving a scale factor K of 18146.2 $(°/h)^{-1}$ at 1548.94nm. The source independent effective PCC data in this PMF coil were extracted first, and the bias drift with above four different light sources estimated and listed in Column 5 of Table 5. It is obvious that sources with narrower spectral width gives bigger error in terms of bias drift. For comparison, the gyro bias drifts were also estimated with the raw PCC data and listed in Column 4 of Table 5. The bias drifts estimated with the raw data are in general ~2 orders of magnitude larger than that with the extracted data. As will be shown later in the next section, the measured bias drift of the FOG with the ~3 km PMF coil is on the order of 0.001°/h, close to the bias drifts estimated with the extracted data.

The distributed PCC of the PMF coil was measured under different temperatures: −30°C, −10°C, + 25°C, + 40°C and + 60°C, by use of the same OCDP system. With the PCC data extraction algorithm in section 3, the location and ratio of the effective PCC points were determined at each of the temperatures. The gyro bias drifts were then estimated with the extracted PCC data with three the different light sources at different temperatures, and the results are plotted in Fig. 10 as the red solid line and circular dots. The bias drift becomes larger at higher or lower temperatures, indicating the PCC is larger at high and low operation temperatures. Better bias drifts were achieved with a source of larger spectral width.
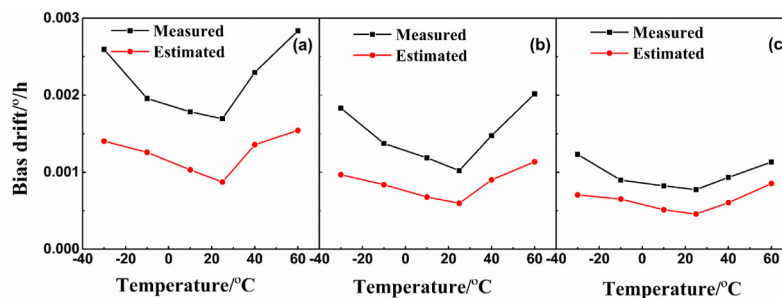

Fig. 10. Estimated and measured bias drift of FOG driven by different sources and under different temperature: (a) SFS1 ($\overline{\lambda}$ = 1531.23nm, Δλ = 6.81nm) (b) SFS2 ($\overline{\lambda}$ = 1563.31nm, Δλ = 13.38nm) (c) SFS3 ($\overline{\lambda}$ = 1544.13nm, Δλ = 27.62nm).
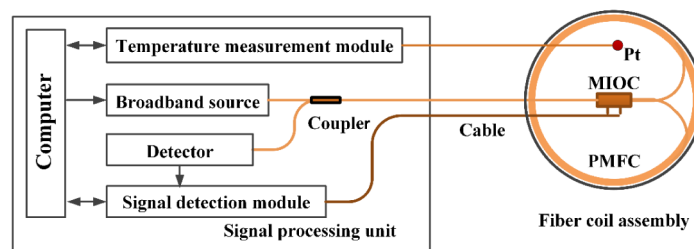
5. Experimental investigation

Fig. 11. Schematic diagram of the experimental gyro setup.

Experiments were conducted to measure the bias drifts of the FOG with the 3-km-long PMF coil. As shown in Fig. 11, the experimental setup comprises of a signal processing unit (SPU) and optical fiber coil assembly. The SPU includes the broadband light source module, a coupler, a detector, a digital closed-loop signal detection module, a temperature measurement

module and a computer for data acquisition. The fiber coil assembly includes a MIOC and the PMF coil and is connected to the SPU by optical fiber/electric cables to form a closed-loop system. The bias drift of the FOG with three different light sources at different temperatures were evaluated experimentally. The temperature of the PMF coil assembly was monitored with a Pt temperature sensor.

The fiber coil assembly was mounted on a temperature controlled rotation stage. The measurements were conducted when the temperature was stabilized at −30°C, −10°C, + 25°C, + 40°C and + 60°C respectively with the three different SFSs with parameters listed in Table 5. The measured results were analyzed with Allan variance curve [19] and the values of the bias drift can be read from the Allan variance curve, as shown in Fig. 12. The bias drifts measurementally experimentally with different light sources at different temperatures are also shown in Fig. 11 as the black solid line and square symbols. It shows that the estimated bias drifts are on the same order as and slightly smaller than the experimentally measured ones, maybe because the phase error due to distributed PCC only contributes partly to the bias drift of the FOG. The experimental results follow the same trend and in general support the prediction of the PCC model and algorithms.
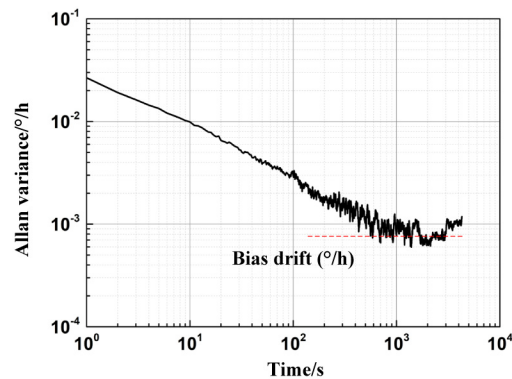

Fig. 12. Typical Allan variance curve.

6. Conclusion

We studied the distributed PCC data in the PMF coil obtained from an OCDP system and developed a model that relates the measured distributed PCC data to that of the "true" PCC ratios and locations in the PMF coil. This model indicates that the measured PCC ratio at each measurement location is the sum of the OCDP source coherence functions centered at a series of discrete PCC points. Based on this model and the characteristics of the measured PCC data, we further developed an algorithm to extract the effective PCC data pairs from the raw measurement data. The extracted data pairs are source independent and may be regarded as the "true" PCC data. We then developed a model and an algorithm to estimate FOG bias drift due to parasitic interference between the coupled waves at the extracted PCC points and the main wave in the PMF coil. The experimental results verify the models and algorithms. The models and algorithms for PCC extraction and FOG bias drift estimation provide a reliable technique to evaluate the quality evaluation of the fiber coil and could be used to quantitatively estimate gyro bias drift. It would be of significance to improve the performance of FOGs.

Funding

References

1. R. Ulrich and M. Johnson, "Fiber-ring interferometer: polarization analysis," Opt. Lett. **4**(5), 152–154 (1979).
2. H. C. Lefèvre, J. P. Bettini, S. Vatoux, and M. Papuchon, "Progress in optical fiber gyroscopes using integrated optics," in Guided Optical Structures in the Military Environment 13 (Advisory Group for Aerospace Research and Development, 1985).
3. D. Zhang, Y. Zhao, W. Fu, W. Zhou, C. Liu, X. Shu, and S. Che, "Nonreciprocal phase shift caused by magnetic-thermal coupling of a polarization maintaining fiber optic gyroscope," Opt. Lett. **39**(6), 1382–1385 (2014).
4. H. C. Lefèvre, "Potpourri of comments about the fiber-optic gyro for its 40th anniversary, and how fascinating it was and it still is," Proc. SPIE **9852**, 985203 (2016).
5. P. Martin, G. Le Boudec, and H. C. Lefèvre, "Test apparatus of distributed polarization coupling in fiber gyro coils using white light interferometry," Proc. SPIE **1585**, 173–179 (1992).
6. K. Takada, J. Noda, and K. Okamoto, "Measurement of spatial distribution of mode coupling in birefringent polarization-maintaining fiber with new detection scheme," Opt. Lett. **11**(10), 680–682 (1986).
7. M. W. Kemmler and H. J. Bueschelberger, "White light interferometry for testing FOG components," Proc. SPIE **1585**, 357–364 (1992).
8. J. Yang, Y. G. Yuan, A. Zhou, J. Cai, C. Li, D. K. Yan, S. Huang, F. Peng, B. Wu, Y. Zhang, Z. H. Liu, and L. B. Yuan, "Full evaluation of polarization characteristics of multifunctional integrated optic chip with high accuracy," J. Lightwave Technol. **32**(22), 4243–4252 (2014).
9. J. N. Chamoun and M. J. F. Digonnet, "Noise and bias error due to polarization coupling in a Fiber Optic Gyroscope," J. Lightwave Technol. **33**(13), 2839–2847 (2015).
10. Z. Ding, Z. Meng, X. S. Yao, X. Chen, T. Liu, and M. Qin, "Accurate method for measuring the thermal coefficient of group birefringence of polarization-maintaining fibers," Opt. Lett. **36**(11), 2173–2175 (2011).
11. J. Yang, Y. Yuan, B. Wu, A. Zhou, and L. Yuan, "Higher-order interference of low-coherence optical fiber sensors," Opt. Lett. **36**(17), 3380–3382 (2011).
12. A. E. Afifi, A. R. El-Damak, T. A. Ramadan, and M. H. Ahmed, "Fiber optical coherence domain polarimetry for PM Fiber measurements," J. Lightwave Technol. **35**(16), 3569–3576 (2017).
13. D. Song, Z. Wang, X. Chen, H. Zhang, and T. Liu, "Influence of ghost coupling points on distributed polarization crosstalk measurements in high birefringence fiber and its solution," Appl. Opt. **54**(8), 1918–1925 (2015).
14. Z. Li, Z. Meng, X. Chen, T. Liu, and X. S. Yao, "Method for improving the resolution and accuracy against birefringence dispersion in distributed polarization cross-talk measurements," Opt. Lett. **37**, 2775–2777 (2012).
15. Z. Yang, J. Yang, H. L. Zhang, H. Y. Li, F. Peng, Y. G. Yuan, Y. Q. Cheng, and L. B. Yuan, "An improved calibration method using third order polarization mode crosstalk for optical coherence domain polarimetry," Proc. SPIE **10323**, 103238E (2017).
16. Z. H. Li, X. S. Yao, X. J. Chen, H. X. Chen, Z. Meng, and T. G. Liu, "Complete characterization of polarization-maintaining measuring fibers using distributed polarization analysis," J. Lightwave Technol. **33**(2), 372–380 (2015).
17. Y. Yuan, D. Lu, J. Yang, J. Wang, H. Li, Z. Yu, H. Zhang, F. Peng, Z. Liu, and L. Yuan, "Range extension of the optical delay line in white light interferometry," Appl. Opt. **56**(16), 4598–4605 (2017).
18. Z. J. Yu, J. Yang, Y. G. Yuan, F. Peng, H. Y. Li, C. B. Hou, C. C. Hou, Z. H. Liu, and L. B. Yuan, "High resolution distributed dispersion characterization for polarization maintaining fiber based on a close-loop measurement framework," IEEE Photonics J. **9**(3), 7103508 (2017).
19. H. C. Lefèvre, *Fiber-Optic Gyroscope* (Artech House, 1993), pp. 92–96, 103–110, 206–218.